Monthly Notices of the ROYAL ASTRONOMICAL SOCIETY

MNRAS **517,** 5617–5626 (2022) https://doi.org/10.1093/mnras/stac3059
Advance Access publication 2022 October 26

Optical studies of a bright Type Iax supernova SN 2020rea

Mridweeka Singh,[1★] Kuntal Misra,[2★] Devendra K. Sahu,[1★] Bhavya Ailawadhi,[2,3] Anirban Dutta,[1,4] D. Andrew Howell,[5,6] G. C. Anupama,[1] K. Azalee Bostroem,[7] Jamison Burke,[5,6] Raya Dastidar,[8,9] Anjasha Gangopadhyay,[10] Daichi Hiramatsu,[5,6,11,12] Hyobin Im,[13,14] Curtis McCully,[5,6] Craig Pellegrino,[5,6] Shubham Srivastav[15] and Rishabh Singh Teja[1,4]

[1]*Indian Institute of Astrophysics, II Block, Koramangala, Bengaluru 560 034, India*
[2]*Aryabhatta Research Institute of Observational Sciences, Manora Peak, Nainital 263 001, India*
[3]*Deen Dayal Upadhyaya Gorakhpur University, Gorakhpur 273009, India*
[4]*Pondicherry University, R.V. Nagar, Kalapet, Puducherry 605014, India*
[5]*Las Cumbres Observatory, 6740 Cortona Drive, Suite 102, Goleta, CA 93117, USA*
[6]*Department of Physics, University of California, Santa Barbara, CA 93106, USA*
[7]*DiRAC Institute, Department of Astronomy, University of Washington, Box 351580, U.W., Seattle, WA 98195, USA*
[8]*Millennium Institute of Astrophysics (MAS), Nuncio Monsenor Sòtero Sanz 100, Providencia, Santiago, Chile*
[9]*Departamento de Ciencias Fisicas, Universidad Andres Bello, Fernandez Concha 700, Las Condes, Santiago, Chile*
[10]*Hiroshima Astrophysical Science Center, Hiroshima University, Higashi-Hiroshima, Japan*
[11]*Center for Astrophysics | Harvard & Smithsonian, 60 Garden Street, Cambridge, MA 02138, USA*
[12]*The NSF AI Institute for Artificial Intelligence and Fundamental Interactions , Cambridge, MA 02139-4307, USA*
[13]*Korea Astronomy and Space Science Institute, 776 Daedeokdae-ro, Yuseong-gu, Daejeon 34055, Republic of Korea*
[14]*Korea University of Science and Technology (UST), 217 Gajeong-ro, Yuseong-gu, Daejeon 34113, Republic of Korea*
[15]*Astrophysics Research Centre, School of Mathematics and Physics, Queen's University Belfast, Belfast BT7 1NN, UK*

Accepted 2022 October 20. Received 2022 October 20; in original form 2022 March 16

ABSTRACT

We present optical photometric and spectroscopic analysis of a Type Iax supernova (SN) 2020rea situated at the brighter luminosity end of Type Iax supernovae (SNe). The light curve decline rate of SN 2020rea is $\Delta m_{15}(\mathrm{g}) = 1.31 \pm 0.08$ mag which is similar to SNe 2012Z and 2005hk. Modelling the pseudo-bolometric light curve with a radiation diffusion model yields a mass of ^{56}Ni of 0.13 ± 0.01 M$_\odot$ and an ejecta mass of $0.77^{+0.11}_{-0.21}$ M$_\odot$. Spectral features of SN 2020rea during the photospheric phase show good resemblance with SN 2012Z. TARDIS modelling of the early spectra of SN 2020rea reveals a dominance of Iron Group Elements (IGEs). The photospheric velocity of the Si II line around maximum for SN 2020rea is ~ 6500 km s^{-1} which is less than the measured velocity of the Fe II line and indicates significant mixing. The observed physical properties of SN 2020rea match with the predictions of pure deflagration model of a Chandrasekhar mass C–O white dwarf. The metallicity of the host galaxy around the SN region is $12 + \log(\mathrm{O/H}) = 8.56 \pm 0.18$ dex which is similar to that of SN 2012Z.

Key words: techniques: photometric – techniques: spectroscopic – supernovae: general – supernovae: individual: SN 2020rea – galaxies: individual: UGC 10655.

1 INTRODUCTION

Type Iax supernovae (SNe) are low luminosity and less energetic cousins of Type Ia SNe (Li et al. 2003; Foley et al. 2013). Type Iax SNe are known to have a wide range of luminosities ($M_r = -12.7$ mag; Karambelkar et al. 2021 to $M_V = -18.4$ mag; Narayan et al. 2011). There are bright members such as SNe 2011ay (Szalai et al. 2015; Barna et al. 2017), 2012Z (Stritzinger et al. 2015) and faint members like SNe 2008ha (Foley et al. 2009; Valenti et al. 2009), 2010ae (Stritzinger et al. 2014), 2019gsc (Srivastav et al. 2020; Tomasella et al. 2020), and 2021fcg (Karambelkar et al. 2021). However, dominance of relatively faint Type Iax SNe can be seen over bright ones (Li et al. 2011; Graur et al. 2017). Though the sample size of Type Iax SNe is increasing with new discoveries by ongoing transient surveys, the progenitor and explosion mechanism of these peculiar objects are still debated. In order to understand them in a better way, detailed study of individual candidates is important.

The pre-maximum spectra of Type Iax SNe are dominated by Intermediate Mass Elements (IMEs), Iron Group Elements (IGEs), along with C and O features. The pre-maximum spectral features are similar to SN 1991T-like Type Ia SNe (Foley et al. 2013; McCully et al. 2014b) with weak Si II, S II, Ca II lines and strong high excitation features such as Fe III. Measured expansion velocities of Type Iax SNe close to maximum lie between 2000 and 8000 km s^{-1} (Foley et al. 2009; Stritzinger et al. 2014) which is significantly less than the expansion velocities associated with Type Ia SNe ($\sim$11 000 km s^{-1}, Wang et al. 2009; Foley et al. 2013). Type Iax SNe show different

★ E-mail: yashasvi04@gmail.com (MS); kuntal@aries.res.in (KM); dks@iiap.res.in (DKS)

spectroscopic behaviour, especially at nebular phase with presence of permitted Fe II lines (Sahu et al. 2008; Jha 2017).

The progenitor system of these explosions are not yet fully understood. Deep pre-explosion images are available for a few Type Iax SNe. In the case of SN 2012Z, the analysis of the pre-explosion image led McCully et al. (2014a) to suggest that the most favoured progenitor of this class could be a white dwarf in a binary system with Helium star as a companion. Nevertheless, the possibility of a single star as the progenitor was not completely ruled out in their work. Based on the pre-explosion images of SN 2014dt, Foley et al. (2015) suggested that a C–O white dwarf in association with a Helium star can be a plausible progenitor system. Moreover, possible detection of Helium features in SNe 2004cs and 2007J were presented by Foley et al. (2013). Detailed spectroscopic studies for a sample of Type Iax SNe, however, resulted in null detection of Helium feature (White et al. 2015; Jacobson-Galán et al. 2019; Magee et al. 2019). Hence, binary system with a Helium star companion of the progenitor white dwarf is still debated.

The low luminosity and less energetic nature of Type Iax SNe suggest an incomplete disruption of the white dwarf which could lead to a bound remnant. The presence of P-Cygni lines and forbidden lines in the late phase spectra has been attributed to the centrally located optically thick high-density region and optically thin SN ejecta, respectively (Jha et al. 2006; Sahu et al. 2008), suggesting two component structure of the ejecta. Foley et al. (2014) presented late time observations of SN 2008ha and discussed about the possibilities of the remnant detection. The observed IR excess seen in the late time light curves of SN 2014dt (Fox et al. 2016) was explained as arising from a bound remnant with an extended optically thick super-Eddington wind. Based on the late-phase spectroscopic study for a larger sample, Foley et al. (2016) have also proposed a two component model for the ejecta of SNe Iax. The possibility of the presence of a bound remnant in these explosions has also been discussed in McCully et al. (2014b), Shen & Schwab (2017), Vennes et al. (2017), Kawabata et al. (2018), Shen et al. (2018), Raddi et al. (2019), Kawabata et al. (2021), and McCully et al. (2022).

Jordan et al. (2012), Kromer et al. (2013), and Fink et al. (2014) gave different deflagration models of C-O white dwarfs and could reproduce most of the observed features seen in relatively bright Type Iax SNe. A disk detonation associated with the merger of a white dwarf with a neutron star or black hole (Fernández & Metzger 2013) can account for some properties seen in Type Iax SNe. On the other hand, to explain the observed properties of faint Type Iax SNe, several channels e.g. mergers involving C–O and O–Ne white dwarfs (Kashyap et al. 2018), partial deflagration associated with hybrid C–O–Ne white dwarf (Denissenkov et al. 2015; Kromer et al. 2015; Bravo et al. 2016), deflagrations of C–O white dwarfs (Lach et al. 2022), core collapse scenario (Moriya et al. 2010), O–Ne white dwarf and neutron star/black hole mergers (Bobrick et al. 2022), and electron capture SN scenario (Pumo et al. 2009) have been proposed.

In this paper, we present photometric and spectroscopic analysis of a bright Type Iax SN 2020rea. Section 2 mentions the discovery, follow-up, and procedures used to reduce the data of SN 2020rea. A short description on the adopted distance and extinction is presented in Section 3. In Section 4, the photometric properties of SN 2020rea are discussed. The bolometric light curve, its fitting with analytical models to infer the explosion parameters, and the comparison with deflagration models are presented in Section 5. Section 6 provides spectral studies of SN 2020rea and its host galaxy. A comparison of the observed features of SN 2020rea with the proposed explosion scenario for SNe Type Iax is made in Section 7. Finally, a summary of this study is presented at the end of the paper in Section 8.

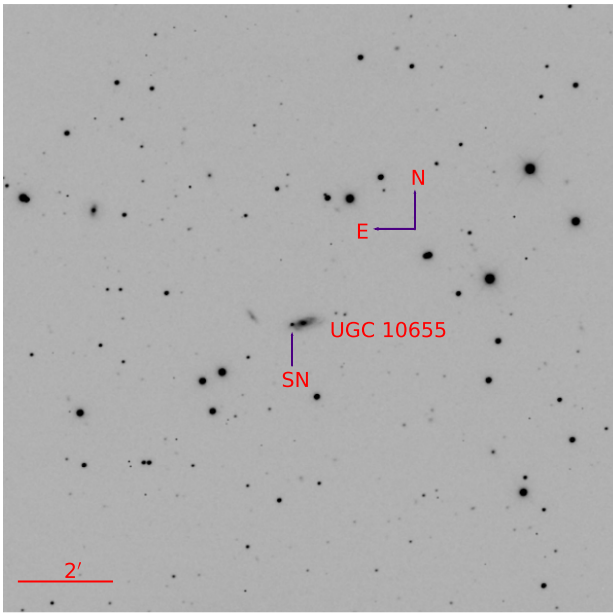

Figure 1. Location of SN 2020rea in UGC 10655. This image is acquired on 2020 August 22 in *V*-band with 1m LCO telescope.

Table 1. SN 2020rea and its host galaxy UGC 10655.

Host galaxy[a]	UGC 10655
Galaxy morphology	Sbc
Redshift	0.02869 ± 0.00015[b]
Helio. radial velocity	8600.15 ± 44.07 km s^{-1}
RA (J2000.0)	$16^{h}59^{m}37\overset{s}{.}82$
Dec. (J2000.0)	$56^{\circ}04'08\overset{''}{.}48$
Galactic extinction $E(B-V)$	0.02 mag
Host extinction $E(B-V)$	0.08 mag[c]
SN type	Iax
Offset from nucleus	$1\overset{''}{.}08$ S $14\overset{''}{.}59$ E
Date of discovery	2020-08-11

Notes. [a]The host galaxy parameters are taken from NED.
[b]Falco et al. (1999).
[c]See Section 3.

2 DISCOVERY, OBSERVATION, AND DATA REDUCTION

SN 2020rea was spotted by Supernova and Gravitational Lenses Follow up (SGLF) team in the Zwicky Transient Facility (ZTF) data (Perez-Fournon et al. 2020) on 2020 August 11 (JD = 2459072.702) in the host galaxy UGC 10655 at a redshift of 0.02869 ± 0.00015 (Falco et al. 1999). It was classified as a Type Ia-pec SN by Poidevin et al. (2020). Fig. 1 shows the location of SN 2020rea in UGC 10655. The details of SN 2020rea and its host galaxy are given in Table 1.

Optical photometric follow-up of SN 2020rea was initiated ∼6 d after discovery with the telescopes of the Las Cumbres Observatory (LCO; Brown et al. 2013) under the Global Supernova Project (GSP) in *BgVri* bands. SN 2020rea is located in the proximity of the host galaxy hence we performed template subtraction to estimate the true SN flux. The templates were observed in *BgVri* bands on 2021 May 27 ∼ 8 months after the discovery. The template subtraction was performed using `PyZOGY` (Guevel & Hosseinzadeh 2017). The `lcogtsnpipe` pipeline (Valenti et al. 2016) was used to estimate the SN magnitudes. Calibration of the instrumental magnitudes

Table 2. Optical photometric observations of SN 2020rea.

Date	JD[a]	Phase[b]	*B* (mag)	*V* (mag)	*g* (mag)	*r* (mag)	*i* (mag)
2020-08-17	78.75	− 5.98	–	18.03 ± 0.05	17.79 ± 0.04	17.95 ± 0.04	18.23 ± 0.03
2020-08-23	84.73	0.00	17.49 ± 0.03	17.40 ± 0.03	17.34 ± 0.03	17.39 ± 0.02	17.65 ± 0.03
2020-09-04	96.71	11.97	18.55 ± 0.07	17.67 ± 0.03	18.20 ± 0.04	17.34 ± 0.02	17.51 ± 0.02
2020-09-08	100.62	15.89	19.27 ± 0.05	18.00 ± 0.04	18.90 ± 0.06	17.79 ± 0.03	17.60 ± 0.01
2020-09-12	104.63	19.99	19.77 ± 0.17	18.28 ± 0.05	19.30 ± 0.10	17.81 ± 0.04	17.72 ± 0.02
2020-09-18	110.68	25.94	20.29 ± 0.32	18.59 ± 0.07	19.66 ± 0.10	18.10 ± 0.05	18.01 ± 0.02
2020-09-22	114.67	29.93	20.24 ± 0.10	18.76 ± 0.09	19.65 ± 0.11	18.31 ± 0.06	18.15 ± 0.03
2020-09-26	118.63	33.89	20.88 ± 0.39	19.03 ± 0.09	19.70 ± 0.14	18.54 ± 0.05	18.37 ± 0.04
2020-09-30	122.63	37.90	20.76 ± 0.40	19.16 ± 0.09	19.91 ± 0.13	18.66 ± 0.08	18.50 ± 0.05
2020-10-07	129.61	44.88	20.90 ± 0.34	19.21 ± 0.12	19.94 ± 0.16	18.86 ± 0.13	18.87 ± 0.05
2020-10-14	136.55	51.81	20.90 ± 0.39	19.44 ± 0.10	20.29 ± 0.22	19.07 ± 0.13	18.91 ± 0.05
2020-10-15	137.55	52.81	20.49 ± 0.32	19.49 ± 0.14	20.11 ± 0.16	18.98 ± 0.10	18.98 ± 0.06
2020-10-20	142.55	57.81	20.73 ± 0.44	19.34 ± 0.12	20.34 ± 0.21	19.17 ± 0.13	19.11 ± 0.08
2020-11-02	155.54	70.81	–	20.02 ± 0.43	–	–	–
2021-01-05	220.03	135.29	–	20.30 ± 0.26	20.49 ± 0.19	20.34 ± 0.26	20.11 ± 0.14
2021-01-09	224.01	139.27	20.61 ± 0.24	20.18 ± 0.17	–	–	–

Notes. [a]2459000 + [b]with respect to g_{max} = 2459084.74.

Table 3. Log of spectroscopic observations.

Date	Phase[a] (d)	Telescope/Instrument
2020-08-16	− 7.0	FTN/FLOYDS
2020-08-19	− 4.0	FTN/FLOYDS
2020-08-22	− 0.9	FTN/FLOYDS
2020-08-23	0.0	FTN/FLOYDS
2020-09-02	9.9	FTN/FLOYDS
2020-09-13	20.9	FTN/FLOYDS

Note. [a]Phase is calculated with respect to g_{max} = 2459084.74.

were done using APASS catalogue. The calibrated photometric magnitudes of SN 2020rea are listed in Table 2.

Spectroscopic follow up of SN 2020rea was initiated ∼5 d after discovery and lasted ∼1 month, using the FLOYDS spectrograph on the 2m FTN telescopes. FLOYDS spectrograph provides a wavelength range of 3300–11000 Å with resolution ranging between 400 and 700. We have used the `floydsspec`[1] pipeline to perform the spectral reduction. Finally, the spectra were scaled with respect to the photometry and corrected for redshift. The log of spectroscopic observations is presented in Table 3.

3 DISTANCE AND EXTINCTION

Assuming H_0 = 73 km s^{-1} Mpc^{-1}, Ω_m = 0.27, Ω_v = 0.73, and a redshift of 0.02869 ± 0.00015, we estimate the luminosity distance of SN 2020rea to be 120.5 ± 6.7 Mpc. The distance modulus is 35.40 ± 0.12 mag. We quote the error from the HyperLeda data base (Makarov et al. 2014). The Galactic extinction along the line of sight in SN 2020rea is $E(B-V)$ = 0.02 mag (Schlafly & Finkbeiner 2011). SN 2020rea lies in the proximity of the host galaxy and hence extinction due to the host galaxy is also expected. To estimate the extinction due to the host galaxy, we used the equivalent width of Na ID line in the spectra. The initial spectral sequence of SN 2020rea shows the presence of a strong Na ID line. We measured the equivalent width of Na ID line in the spectrum combined using two spectra of SN 2020rea close to maximum (Fig. 6). The estimated equivalent width is 0.66 ± 0.06 Å that translates to $E(B-V)$ = 0.08 ± 0.02 mag, using the relation given in Poznanski, Prochaska & Bloom (2012). Thus, the total extinction due to the combination of the Galactic and host components is $E(B-V)$ = 0.10 ± 0.02 mag (A_V = 0.31 mag assuming R_V = 3.1).

[1]https://www.authorea.com/users/598/articles/6566

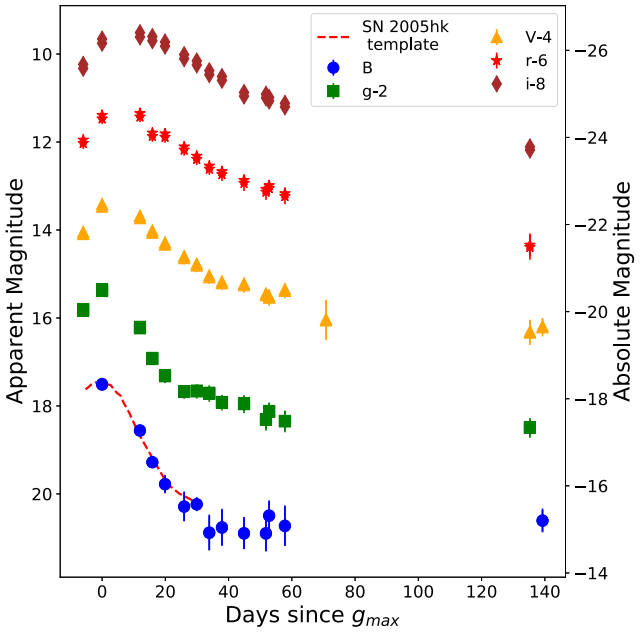

Figure 2. Light-curve evolution of SN 2020rea in *BgVri* bands. The light curves in all bands are shifted for clarity. In the right *Y*-axis, corresponding absolute magnitudes for each band are presented. The template light curve of SN 2005hk used for estimating the peak magnitude and time of SN 2020rea in *B* band is also shown in the figure with dashed line.

4 ANALYSIS OF THE LIGHT CURVE

Fig. 2 shows the light curve evolution of SN 2020rea in *BgVri* bands. The peak phase is well covered in all the bands except *B* band. To estimate the peak time and peak magnitude in *B* band, a chi-

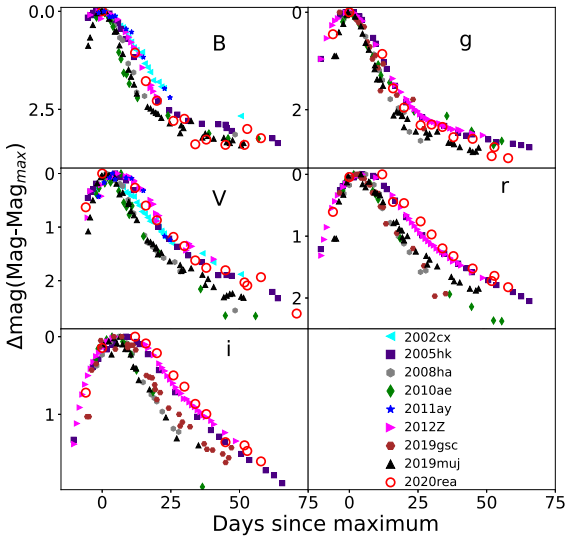

Figure 3. Light curves of SN 2020rea in the *BgVri* bands and its comparison with other Type Iax SNe. Here, comparison plots in *B* and *V* bands are made with respect to maximum in *B* band, while in *gri* bands comparison plots are constructed with respect to *g*-band maximum.

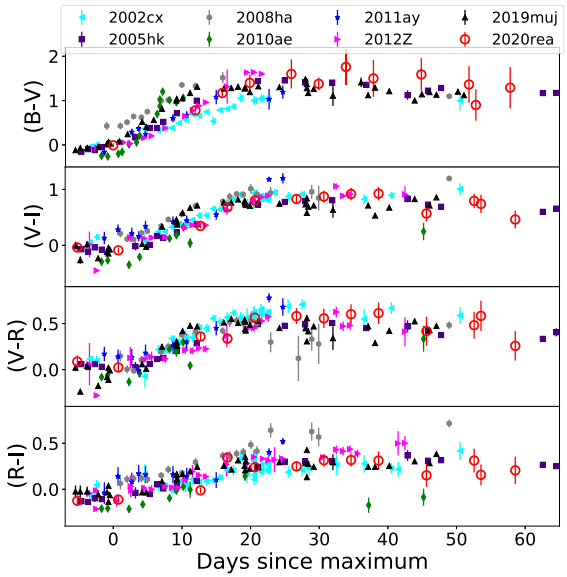

Figure 4. The colour evolution of SN 2020rea and its comparison with colours of other well-studied Type Iax SNe.

square minimization based template fitting method was used and a best match was found with SN 2005hk. The best fit indicates that SN 2020rea peaked at JD $= 2459083.5 \pm 1$ with peak magnitude 17.33 ± 0.07 mag in the *B* band. With these estimates, the light curve decline rate (Δm_{15}) of SN 2020rea in *B* band is 1.61 ± 0.14 mag. In other bands, peak phase and peak time are estimated by fitting a low order spline to the light curve. The respective decline rates (Δm_{15}) in *g*, *V*, *r*, and *i* bands are 1.31 ± 0.08, 0.54 ± 0.05, 0.46 ± 0.05, and 0.50 ± 0.04 mag. The peak in *g* and *V* bands occur on JD $= 2459084.74$ and 2458084.77 at a magnitudes of 17.34 ± 0.03 mag and 17.40 ± 0.03 mag, respectively. We have used *g*-band maximum throughout the paper, as a reference, for further work.

We compare the light-curve characteristics of SN 2020rea with other well studied Type Iax SNe. We have represented the wide luminosity range in choosing the comparison sample which includes SNe 2002cx (Li et al. 2003), 2005hk (Sahu et al. 2008), 2008ha (Foley et al. 2009), 2010ae (Stritzinger et al. 2014), 2011ay (Szalai et al. 2015), 2012Z (Stritzinger et al. 2015; Yamanaka et al. 2015), 2019muj (Barna et al. 2021; Kawabata et al. 2021), and 2019gsc (Srivastav et al. 2020). Fig. 3 exhibits the normalized magnitudes of each SN with respect to the peak magnitude in the respective bands. In *B*-band, SN 2020rea declines faster than SNe 2002cx, 2011ay and follows a similar evolution as SNe 2005hk and 2012Z up to $\sim$ 20 d after maximum, whereas it declines faster than SN 2005hk at later epochs and shows similarity with SN 2019muj. In *V*-band, SN 2020rea shows resemblance with SNe 2005hk and 2012Z. The early time evolution of *g*-band light curve of SN 2020rea (Δm_{15}(g) $= 1.31 \pm 0.08$ mag) is similar to SNe 2005hk [Δm_{15}(g) $= 1.36 \pm 0.01$ mag, Stritzinger et al. (2015)] and 2012Z [Δm_{15}(g) $= 1.31 \pm 0.01$ mag, Stritzinger et al. (2015)], whereas in *r*-band SN 2020rea (Δm_{15}(r) $= 0.46 \pm 0.05$ mag) declines slightly slower than SNe 2005hk [$\Delta m_{15}(r) = 0.70 \pm 0.02$ mag; Stritzinger et al. (2015)] and 2012Z [$\Delta m_{15}(r) = 0.66 \pm 0.02$ mag, Stritzinger et al. (2015); Fig. 3]. In *i* band, SN 2020rea (Δm_{15}(i) $= 0.50 \pm 0.04$ mag) shows similarity with SN 2012Z [Δm_{15}(i) $= 0.54 \pm 0.04$ mag, Stritzinger et al. 2015) and declines slower than SN 2005hk [Δm_{15}(i) $= 0.60 \pm 0.01$ mag; Stritzinger et al. 2015].

Fig. 4 presents reddening corrected *(B − V)*, *(V − I)*, *(V − R)*, and *(R − I)* colour evolution of SN 2020rea and its comparison with other Type Iax SNe. For SNe 2020rea and 2010ae, we have used the formulations given in Jordi, Grebel & Ammon (2006) to convert *ri* magnitude into *RI* magnitude. The *(B – V)*, *(V – I)*, *(V – R),* and *(R – I)* colour evolution of SN 2020rea follows a trend similar to other Type Iax SNe used for comparison. We have used date of *B*-band maximum as reference for SNe 2002cx and 2011ay and *g*-band maximum as reference for all the other SNe used for comparison.

Using the distance and extinction given in Section 3, we estimate the peak absolute magnitude of SN 2020rea in *V* band $= -18.30 \pm 0.12$ mag. This is similar to SNe 2011ay (Stritzinger et al. 2015), 2012Z (Stritzinger et al. 2015), and higher than SNe 2002cx (Li et al. 2003), 2005hk (Sahu et al. 2008), and 2014dt (Singh et al. 2018). Absolute magnitudes of SN 2020rea in *BgVri* bands are presented in Fig. 2.

5 LIGHT-CURVE MODELLING

We construct the pseudo-bolometric light curve of SN 2020rea, using extinction corrected magnitudes in *BgVri* bands. For the epoch JD 2459078.8, the *B*-band photometry is missing and hence we fit the *B*-band light curve with the template of SN 2005hk (Sahu et al. 2008) to estimate the magnitude. The extinction corrected magnitudes were converted to flux using zero points from the SVO filter profile service [2] (Rodrigo & Solano 2020). These fluxes are used to generate spectral energy distribution (SED) at each epoch which was then integrated using trapezoidal rule between 4000 and 9000 Å to get the pseudo-bolometric flux. The contribution of UV and IR flux to the total bolometric flux is not well constrained for Type Iax SNe. It is estimated to be typically lying in the range of 10–53 per cent (Phillips et al. 2007; Yamanaka et al. 2015; Tomasella et al. 2016, 2020; Srivastav et al. 2020; Dutta et al. 2022). Due to unavailability of data in UV and IR bands, we have used pseudo-bolometric fluxes and reported the lower limit of the explosion parameters.

[2] http://svo2.cab.inta-csic.es/theory/fps/index.php?mode=browse&gname=LCO&asttype =

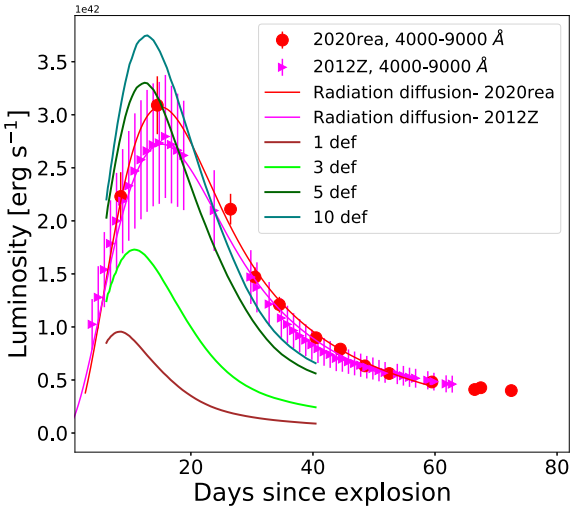

Figure 5. Pseudo-bolometric light curves of SNe 2020rea and 2012Z fitted with the radiation diffusion model are shown. The pseudo-bolometric light curves are compared with optical bolometric light curves of the pure deflagration of M_{ch} white dwarf Fink et al. (2014).

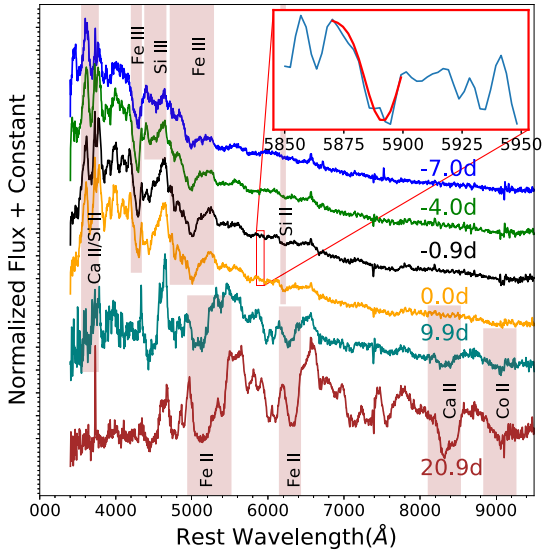

Figure 6. Spectral evolution of SN 2020rea spanning between −7.0 d and + 20.9 d, since maximum in *g* band. Prominent lines are marked with shaded bars. In the inset plot, we have presented the zoomed Na ID feature and the fit associated with it.

The integrated fluxes are converted to luminosity using the distance modulus $\mu = 35.40 \pm 0.12$ mag. The peak pseudo-bolometric luminosity of SN 2020rea is $(3.09 \pm 0.27) \times 10^{42}$ erg s^{-1} and it occurred at JD 2459087.26 about 2.52 d after maximum in *g* band. For direct comparison, we also estimate the pseudo-bolometric light curve of SN 2012Z, using *BgVri* data with $E(B-V) = 0.11 \pm 0.03$ mag (Stritzinger et al. 2015) and distance modulus of 32.34 ± 0.28 mag, obtained using the luminosity distance of 29.4 ± 3.8 Mpc. The peak pseudo-bolometric luminosity of SN 2012Z is $(2.82 \pm 0.58) \times 10^{42}$ erg s^{-1} at JD 2455972.0. The peak pseudo-bolometric luminosity of SN 2020rea is slightly higher than SN 2012Z and lies towards the brighter end of the luminosity distribution of Type Iax SNe. Fig. 5 shows the pseudo-bolometric light curves of SNe 2020rea and 2012Z.

To constrain the amount of ^{56}Ni synthesized during the explosion, we used a radiation diffusion model (Arnett 1982; Valenti et al. 2008; Chatzopoulos, Wheeler & Vinko 2012) that takes into account energy generated through radioactive decay from $^{56}\text{Ni} \rightarrow {}^{56}\text{Co} \rightarrow {}^{56}\text{Fe}$ and also includes grey-ray escape from the ejecta.

The output luminosity is expressed as

$$L(t) = M_{\rm Ni} e^{-x^2}[(\epsilon_{\rm Ni} - \epsilon_{\rm Co}) \int_0^x 2ze^{z^2-2zy}\,dz + \epsilon_{\rm Co} \int_0^x 2ze^{z^2-2yz+2zs}\,dz](1 - e^{-(\frac{t_\gamma}{t})^2}), \quad (1)$$

where t (d) is the time since explosion, $t_{\rm lc}$ is time-scale of the light curve, t_γ is gamma-ray time-scale, $M_{\rm Ni}$ is initial mass of ^{56}Ni, $x \equiv t/t_{\rm lc}$, $y \equiv t_{\rm lc}/(2t_{\rm Ni})$ and $s \equiv [t_{\rm lc}(t_{\rm Co} - t_{\rm Ni})/(2t_{\rm Co}t_{\rm Ni})]$ with $t_{\rm Ni} = 8.8$ d and $t_{\rm Co} = 111.3$ d, respectively. The rate of energy generation due to Ni and Co decay are $\epsilon_{\rm Ni} = 3.9 \times 10^{10}$ erg s^{-1} g^{-1} and $\epsilon_{\rm Co} = 6.8 \times 10^9$ erg s^{-1} g^{-1}, respectively. The free parameters in the model are epoch of explosion $t_{\rm expl}$, $M_{\rm Ni}$, t_γ and $t_{\rm lc}$.

The mass of ejecta ($M_{\rm ej}$) and kinetic energy ($E_{\rm K}$) are expressed as

$$M_{\rm ej} = 0.5\frac{\beta c}{\kappa} v_{\rm exp} t_{lc}^2, \quad (2)$$

$$E_{\rm K} = 0.3 M_{\rm ej} v_{\rm exp}^2, \quad (3)$$

where $v_{\rm exp}$, c and β (= 13.8) are the expansion velocity of the ejecta, the speed of light, and the constant of integration, respectively.

The fit of the radiation diffusion model to the pseudo-bolometric light curve of SN 2020rea gives $^{56}\text{Ni} = 0.13^{+0.01}_{-0.01}$ M$_\odot$, $t_{\rm lc} = 12.36^{+0.9}_{-1.75}$ d, $t_\gamma = 43.60^{+2.4}_{-1.7}$ d, and $\text{JD}_{\rm exp} = 2459070.64^{+1.45}_{-0.76}$. The ejecta mass for SN 2020rea is estimated as $M_{\rm ej} = 0.77^{+0.11}_{-0.21}$ M$_\odot$ and kinetic energy $\text{KE} = 0.19^{+0.02}_{-0.06} \times 10^{51}$ erg, using a constant opacity $\kappa_{\rm opt} = 0.1$ cm^2 g^{-1} and $v_{\rm exp}$ of 6500 km s^{-1}, close to maximum light.

We repeat the same exercise for the pseudo-bolometric light curve of SN 2012Z. We get $^{56}\text{Ni} = 0.12^{+0.01}_{-0.01}$, $t_{\rm lc} = 14.19^{+0.8}_{-1.2}$ d, $t_\gamma = 43.68^{+1.2}_{-1.5}$ d, and $\text{JD}_{\rm exp} = 2455954.39^{+0.5}_{-0.37}$. Using an expansion velocity of 7000 km s^{-1} and the same constant optical opacity, we get $M_{\rm ej} = 1.09^{+0.12}_{-0.19}$ M$_\odot$ and $\text{KE} = 0.32^{+0.04}_{-0.05} \times 10^{51}$ erg. The values of ^{56}Ni mass, ejecta mass, and kinetic energy estimated by Stritzinger et al. (2014) for SN 2012Z are 0.25–0.29 M$_\odot$, 1.4–2.6 M$_\odot$, and 0.7–2.8 $\times$ 10^{51} erg, respectively, which are higher than our estimates. The difference is mostly due to the adopted distance modulus, the wavelength range of the SED and velocity used for estimating the explosion parameters. The faster rise in SN 2020rea as compared to SN 2012Z could be attributed to the different amount of ^{56}Ni mixing in the ejecta.

We compare the pseudo-bolometric light curves of SN 2020rea and SN 2012Z with optical bolometric light curves of pure deflagration model of $M_{\rm ch}$ white dwarfs (Fink et al. 2014). For each model mentioned in Fig. 5, we integrate the model optical spectrum at each epoch available with the HESMA data base in the same wavelength range as for SN 2020rea to obtain the model pseudo-bolometric luminosity. In the deflagration models, the explosion strength is characterized by ignition spots. With the increase in number of ignition spots, more material burns, which leads to an increase in the luminosity, explosion energy, and ejecta velocity. The model light curves for N1-def, N3-def, N5-def, and N10-def, with ignition spots 1, 3, 5, 10, respectively, are shown in Fig. 5.

The early photospheric phase of the light curve for SN 2020rea falls between models N3-def and N5-def. However, the observed light curves of both SNe 2012Z and 2020rea declines slower than the N5-def as well as the N10-def model bolometric light curves. This is because the ejected mass, the parameter that accounts for

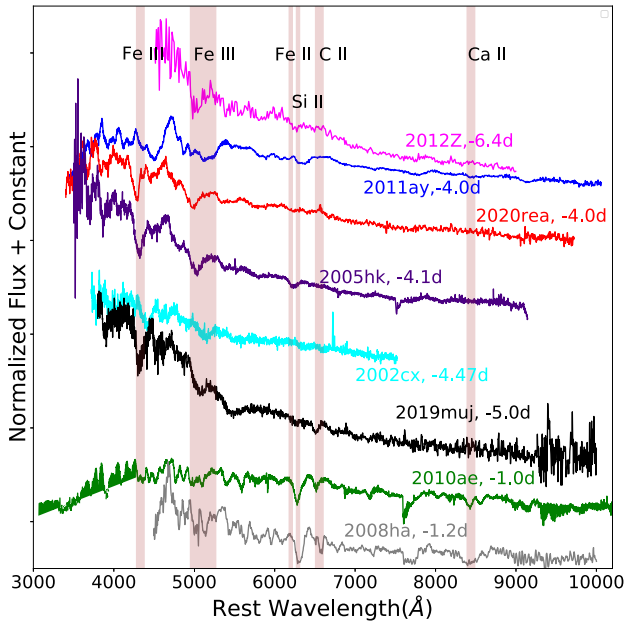

Figure 7. Comparison of pre-maximum spectrum of SN 2020rea with other well studied Type Iax SNe.

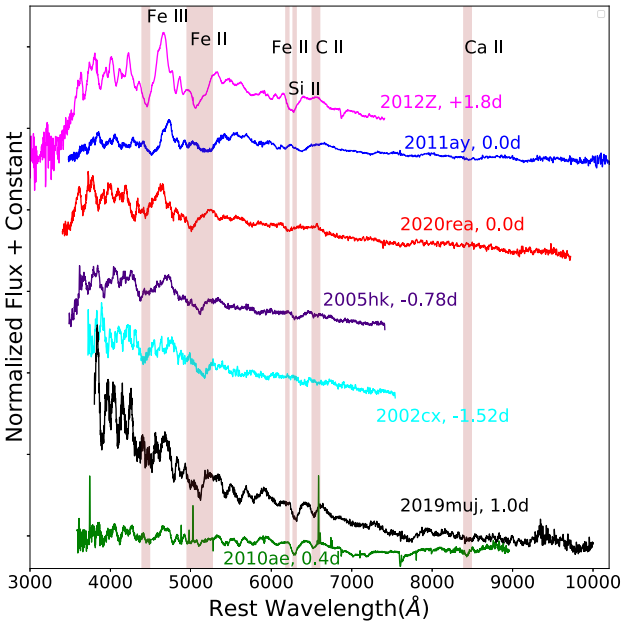

Figure 8. Near maximum spectrum of SN 2020rea is shown with spectra of other Type Iax SNe at comparable epochs.

the decline rate, in the N5-def and N10-def models are 0.372 and 0.478 $M_{\odot}$, respectively (Fink et al. 2014), which are less than the estimated ejecta mass for SNe 2012Z and 2020rea.

6 SPECTRAL PROPERTIES

Fig. 6 presents the spectral evolution of SN 2020rea from ~ -7 to $+21$ d. The early time spectra are dominated by a blue continuum along with well developed P-Cygni profiles with relatively broad absorption features. The pre-maximum spectra of SN 2020rea show Si II/Ca II feature in the blue region, Fe III, Si III, S II, and relatively weak Si II feature around 6000 Å. The spectrum around maximum is similar to the pre-maximum spectra with an evolved Si II feature. After maximum, a feature at ∼6000 Å grows stronger and can be associated with Fe II. In the 8000 to 9000 Å region, the Ca II NIR triplet starts developing. A clear absorption feature due to Co II ∼ 9000 Å is also present. The spectral region between 5500 and 7000 Å is dominated by Fe II lines. By $+21$ d the continuum becomes redder and Co II around 6600 Å starts developing. In addition, Fe II feature in the blue region, Ca II NIR triplet and Co II at ∼9000 Å become stronger.

6.1 Comparison with other Type Iax SNe

To investigate the nature of spectral lines, we compare the pre-maximum, near maximum, and post-maximum spectra of SN 2020rea with other well studied Type Iax SNe such as SNe 2002cx (Li et al. 2003), 2005hk (Phillips et al. 2007; Sahu et al. 2008), 2008ha (Valenti et al. 2009; Foley et al. 2009), 2010ae (Stritzinger et al. 2014), 2011ay (Foley et al. 2013), 2012Z (Foley et al. 2013; Stritzinger et al. 2015), and 2019muj (Barna et al. 2021). Fig. 7 presents the pre-maximum spectra of SN 2020rea and other Type Iax SNe. The Fe III feature near 4000 and 5000 Å are seen in all the SNe having coverage in bluer region. The C II feature is prominent in fainter and intermediate luminosity Type Iax SNe 2008ha, 2010ae and 2019muj, however, in SN 2020rea and other bright Type Iax SNe, this feature is very weak. The Ca II NIR triplet can only be seen in SNe

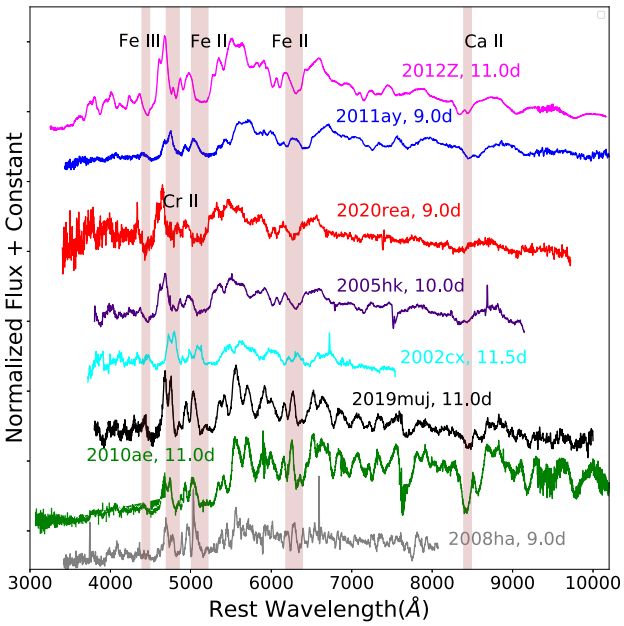

Figure 9. The post-maximum spectrum of SN 2020rea compared with spectra of other Type Iax SNe at similar epoch.

2008ha and 2010ae. Overall, pre-maximum spectroscopic features of SN 2020rea are typical of brighter Type Iax SN. In the spectral comparison near maximum, we find that the prominent spectral lines such as Fe III, Fe II, and Si II are present in all the SNe as shown in Fig. 8. In the post maximum spectra (Fig. 9), the Ca II NIR feature is clearly seen in SNe 2005hk, 2010ae, 2011ay, 2012Z, and 2019muj. SN 2020rea has weak Ca II NIR triplet. The Fe III, Fe II multiplets, and Cr II lines are clearly visible in all the SNe. At the post maximum phase, SNe 2020rea and 2012Z show resemblance in their spectral properties. For a detailed spectral comparison between SNe 2012Z and 2020rea, spectra obtained ∼20 d after maximum of both the SNe

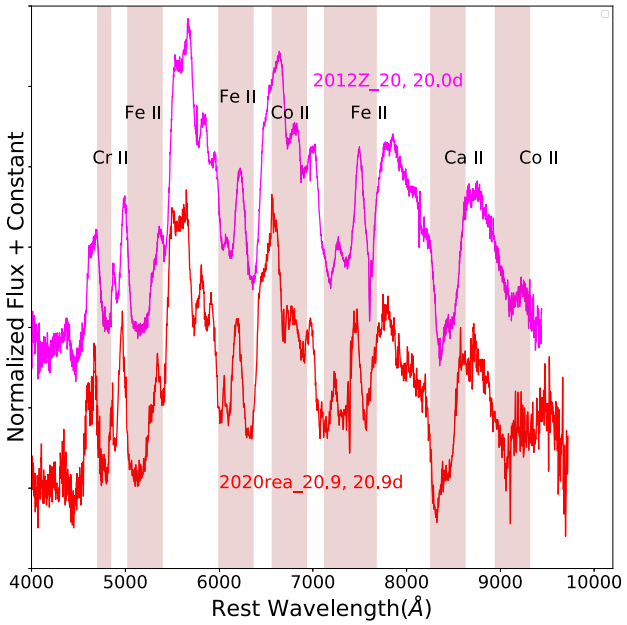

Figure 10. Comparison of spectral features of SN 2020rea at + 21 d with SN 2012Z.

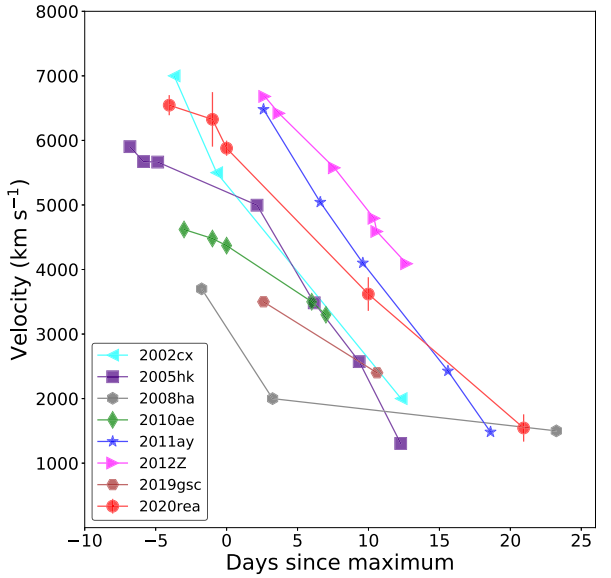

Figure 11. Velocity evolution of Si II line of SN 2020rea and its comparison with other well-studied Type Iax SNe. Error bars associated with velocity estimation of SN 2020rea are also plotted in the figure.

are plotted in Fig. 10. We notice that both the SNe show similarities with each other in terms of spectral signatures, displaying relatively broad features.

Fig. 11 shows the velocity evolution of the Si II 6355 Å feature of SN 2020rea and other Type Iax SNe. The line velocities are measured by fitting Gaussian profiles to the absorption minima of the P-Cygni profile associated with Si II line. The error bar associated with velocities of SN 2020rea are measurement errors only. In the pre-maximum phase, the line velocity of the Si II feature in SN 2020rea is less than SN 2002cx and higher than SN 2005hk. In the post-maximum phases the Si II line velocity of SN 2020rea is lower than SNe 2011ay, 2012Z, and higher than other comparison SNe. In the late post-maximum phase, the identification of Si II is a bit questionable as Fe II lines (at 6149 and 6247 Å) start appearing close to the Si II line.

The velocity of the Fe II 5156 Å line in the pre-maximum and near maximum spectra are estimated as ∼10 000 and 8570 km s^{-1}, respectively, which are around 3500 and 2000 km s^{-1} higher than the Si II velocity at similar phase. This trend of higher velocity of Fe II lines as compared to Si II line shows significant mixing of burned materials (Phillips et al. 2007).

6.2 Spectral modelling

We perform modelling of a few spectra of SN 2020rea, using TARDIS (a one dimensional radiative transfer code, Kerzendorf & Sim 2014; Kerzendorf et al. 2018). TARDIS assumes an opaque core with a sharp boundary or photosphere that emits a blackbody continuum. The ejecta is divided into spherical shells and is assumed to be undergoing homologous expansion. TARDIS allows the user to supply custom density and abundance profiles for the SN ejecta as input. In this work, we assume a uniform abundance profile for each element. The other input parameters are time since explosion and luminosity at a comparable epoch of the spectrum. The photospheric approximation used in TARDIS means that it is only applicable at early times. To generate the synthetic spectrum, we use as input the bolometric luminosity at the corresponding epoch. The mass fractions of radioactive isotopes are varied to improve the fit. For SN ejecta, we adopt an exponential density profile of the form

$$\rho(v, t_{\rm exp}) = \rho_0 \left(\frac{t_0}{t_{\rm exp}}\right)^3 e^{-v/v_0} \quad (4)$$

where t_0 = 2 d, ρ_0 is reference density (= 6 × 10^{-11} g cm^{-3}), $t_{\rm exp}$ is time since explosion, v is velocity, and v_0 is the reference velocity.

In order to perform the TARDIS spectral fitting we adopt v_0 = 7000 km s^{-1} and explosion time $t_{\rm exp}$ JD = 2459070 (see Section 5 for details). The outer velocity of the ejecta has been fixed at 11 500 km s^{-1} and the inner velocity was varied between 6800 and 6000 km s^{-1}. Since there is degeneracy in the parameters used in TARDIS fit, the spectral model presented in this paper is not unique. The modelled spectra for −4.0, 0.0, and + 9.9 d with respect to g-band maximum are overplotted on the observed spectrum in Fig. 12. To model the observed spectra, species of carbon, oxygen, iron, cobalt, calcium, chromium, titanium and other ions usually present in SN ejecta are used. As we did not detect lines due to helium in the spectra, helium is not included in the model.

Table 4 presents the mass fraction of the dominant elements used to generate the model spectra (Fig. 12). In the modelled spectrum at −4.0 d, Fe features between 4000 and 5000 Å are well reproduced, Si II line is weak and continuum matches well with the observed spectrum. To constrain mass fraction of Si, synthetic spectra were generated by varying Si mass fraction at different epochs. It is found that increasing Si mass fraction beyond 1 per cent for pre-peak spectrum and 3 per cent for post-peak spectrum degrades the fit. Hence, we have used 2 per cent of Si for spectral fitting at all the three epochs. We do not see strong features due to C and O in the spectra, usually they are used as filler elements. However, we do see a weak O I line in the spectrum obtained at maximum and +9.9 d. We have used a significant amount of Ni for fitting all three spectra of SN 2020rea presented in Fig. 12. In the synthetic spectra at pre-maximum and at maximum a very low amount of Fe is used as introducing more Fe resulted in over represented Fe features. We have included ∼20 per cent Neon as a filler element for fitting the first two epochs and ∼ 2 per cent of Ne for fitting the last spectrum

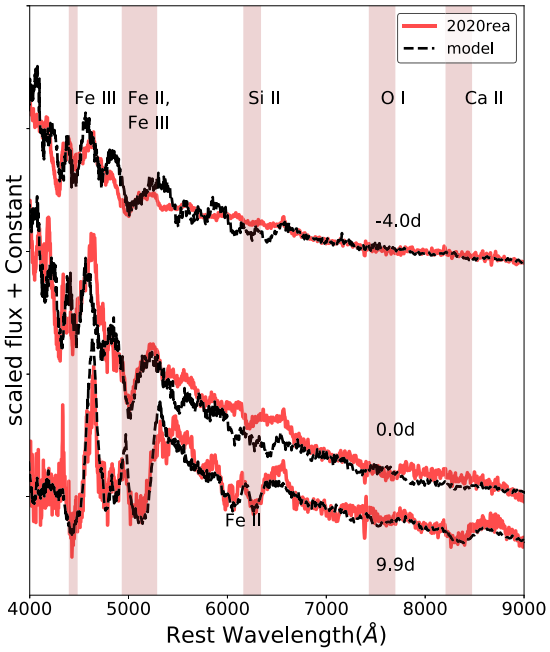

Figure 12. Spectra of SN 2020rea during the photospheric phase, overplotted are the model spectra generated using TARDIS.

at +9.9 d since maximum. IMEs such as Mg, Ca, and S are also used to fit the spectra. In the modelled spectrum around maximum, the region between 4000 and 5200 Å is similar to the observed spectrum. In the +9.9 d spectrum, the observed spectral features and continuum are well reproduced by the model with significant amount of IGEs. However, the 'W' feature at ∼6000 Å could not be reproduced. This feature is attributed to the presence of S line during the early phase of evolution which is later converted to iron when the SN enters the Fe dominated phase. Since we have assumed a model with a uniform abundance profile for each element and got a fairly good fit for our +9.9 d spectrum, this indicates towards a well-mixed ejecta, which is expected in a deflagration scenario (Gamezo et al. 2003).

6.3 Host galaxy metallicity

We have calculated the metallicity of the host galaxy of SN 2020rea, using narrow emission line fluxes in the host galaxy spectrum taken on 2020 August 15 with LCO's FLOYDS spectrograph at Faulkes Telescope North (FTN). Prominent lines of H α, [N II], etc., are present in the host spectrum. There are several methods to measure the metallicity (McGaugh 1991; Kewley & Dopita 2002; Pettini & Pagel 2004; Pilyugin & Thuan 2005). These calculations involve flux measurements of various emission lines. Using the N2 index calibration of Pettini & Pagel (2004), we estimate the metallicity of the host galaxy as 12 + log(O/H) = 8.56 ± 0.18 dex. This is comparable to the metallicity of the host galaxy of SNe 2012Z (8.51 ± 0.31 dex; Yamanaka et al. 2015) and 2020sck (8.54 ± 0.05 dex; Dutta et al. 2022). The metallicity measurements for host galaxy of faint Type Iax SNe such as SNe 2008ha, 2010ae, 2019gsc, 2020kyg are 8.16 ± 0.15 dex (Foley et al. 2009), 8.40 ± 0.18 dex (Stritzinger et al. 2014), 8.10 ± 0.06 dex (Srivastav et al. 2020), and 8.68 ± 0.04 dex (Srivastav et al. 2022), respectively. Magee et al. (2017) demonstrated that there is no clear correlation between host galaxy metallicity and SN luminosity for Type Iax SNe; however, with the increased sample, we do see a tendency of Type Iax SNe to prefer metal poor hosts.

7 EXPLOSION SCENARIO

SN 2020rea is one of the brightest members of Type Iax sub-class. In order to understand, the most favorable explosion scenario for SN 2020rea, we compare the observational properties of SN 2020rea with different models one by one.

First, we consider the pulsational delayed detonation (PDD) model. In the PDD scenario, the white dwarf remains bound while expanding due to slow deflagration and after that detonation occurs during pulsation because of compression and ignition caused by infalling C–O layers (Ivanova, Imshennik & Chechetkin 1974; Khokhlov 1991a, c; Khokhlov, Mueller & Hoeflich 1993; Hoeflich, Khokhlov & Wheeler 1995; Hoeflich & Khokhlov 1996; Bravo & García-Senz 2006; Baron et al. 2012; Dessart et al. 2014). In the PDD explosion of an M_{ch} C–O white dwarf, Fe group elements are produced in the deflagration phase. The mass of ^{56}Ni produced in these model falls in between 0.12 and 0.66 $M_\odot$ (Hoeflich et al. 1995). The estimated ^{56}Ni mass for SN 2020rea matches with PDD5 model (Hoeflich et al. 1995), but ejecta velocity for SN 2020rea (∼6500 km s^{-1}) is lower than that predicted by PDD5 model (8400 km s^{-1}). Also, the observed $(B - V)_0$ colour at maximum (−0.01 mag) for SN 2020rea does not match with the $(B - V)_0$ colour of PDD5 model (0.44 mag; Hoeflich et al. 1995).

Secondly, we consider a low-energy core-collapse explosion model of a massive star which has been used to explain the observational features of some faint Type Iax SNe such as SN 2008ha (Valenti et al. 2009; Foley et al. 2009; Moriya et al. 2010). Because of the low energy budget of faint SNe, a considerable amount of the ejecta falls back on to the remnant. This core-collapse scenario predicts kinetic energy of 1.2 × 10^{48} erg, 0.074 $M_\odot$ of ejecta mass and 0.003 $M_\odot$ of ^{56}Ni (Moriya et al. 2010). Thus, the predicted parameters in the core-collapse scenario are in disagreement with those of SN 2020rea.

Next, we investigate the deflagration to detonation transition (DDT) model (Khokhlov 1991a, b; Khokhlov et al. 1993; Hoeflich et al. 1995; Hoeflich & Khokhlov 1996; Höflich et al. 2002; Seitenzahl et al. 2013; Sim et al. 2013) that has been used to explain several observational properties of Type Ia SNe by varying the central density of white dwarf and strength of deflagration. The

Table 4. Parameters used in TARDIS model for SN 2020rea.

t^a (d)	L (log $L/L_\odot$)	v_{inner} (km s^{-1})	X(Si)	X(C)	X(O)	X(S)	X(Ni)	X(Ca)	X(Co)	X(Fe)	X(Ne)	X(Mg)	X(Cr)	X(Ti)
−4.0	8.9	6800	0.02	0.02	0.10	0.004	0.4	0.003	0.006	0.00005	0.20695	0.04	0.18	0.01
0.0	9.15	6500	0.02	0.02	0.10	0.004	0.4	0.003	0.006	0.0005	0.2065	0.04	0.18	0.01
9.9	8.99	6000	0.02	0.02	0.10	0.004	0.4	0.003	0.005	0.35	0.018	0.04	0.02	0.01

Note. [a]With respect to g_{max} = 2459084.74.

basic assumption in the deflagration to detonation models is that at late stage of explosion there is a transition of deflagration flame into a detonation front. DDT models (Seitenzahl et al. 2013; Sim et al. 2013) are generated by varying the number of ignition points. The mass of ^{56}Ni produced by these models (0.32–1.1 $M_\odot$; Sim et al. 2013) is very high as compared to the ^{56}Ni produced in SN 2020rea explosion. The range of kinetic energy (E_k = 1.20–1.67 × 10^{51} erg), absolute magnitude in *B* band (−19.93 to −18.16 mag), and the redder $(B - V)_0$ colour at maximum (0.15–0.56 mag) of the DDT models (Sim et al. 2013) do not agree with the estimated parameters of SN 2020rea.

Finally, we take into account the three-dimensional pure deflagration of a C–O white dwarf (Fink et al. 2014) that can successfully explain the observed properties of the bright and intermediate luminosity Type Iax SNe. These models provide a wide range of ^{56}Ni mass between 0.03 and 0.38 $M_\odot$, rise time between 7.6 and 14.4 d, and peak *V*-band absolute magnitudes spanning between −16.84 and −18.96 mag (Fink et al. 2014). The observed parameters of SN 2020rea (^{56}Ni mass = 0.13 ± 0.01 $M_\odot$, rise time = ∼ 16 d, *V*-band peak absolute magnitude = −18.30 ± 0.12 mag) fall within the range prescribed by these models. In Section 5, we compared the pseudo-bolometric light curve of SN 2020rea with optical bolometric light curves presented in Fink et al. (2014). The mixed abundance distribution given by these models is consistent with SN 2020rea. The expansion velocity inferred from Fe line is higher than Si lines, indicating significant mixing in the ejecta. Furthermore, modelling the spectra of SN 2020rea with TARDIS (Section 6.2) suggests a mixed distribution of elements, consistent with the deflagration scenario.

8 SUMMARY

The photometric and spectroscopic investigations of SN 2020rea in optical wavelengths show that it lies at the brighter end of Type Iax luminosity distribution. The light curve decline rate in *B* and *g* bands are $\Delta m_{15}(B) = 1.61 \pm 0.14$ mag and $\Delta m_{15}(g) = 1.31 \pm 0.08$ mag, respectively, indicating its similarity with SNe 2005hk and 2012Z. The colour evolution of SN 2020rea is analogous to other Type Iax SNe. Modelling of the pseudo-bolometric light curve (constructed using *BgVri* bands) places SN 2020rea in the category of relatively bright Type Iax SNe with a rise time of ∼16 d and ^{56}Ni of 0.13 ± 0.01 $M_\odot$. Assuming a photospheric velocity of 6500 km s^{-1}, ejecta mass and kinetic energy are estimated to be $0.77^{+0.11}_{-0.21}$ $M_\odot$ and $0.19^{+0.02}_{-0.06} \times 10^{51}$ erg, respectively. The comparison of the pseudo-bolometric light curve of SN 2020rea with optical bolometric light curves representing deflagration models of varying strength shows that the light curve of SN 2020rea is situated between N3-def and N5-def models during the early photospheric phase. The post-peak decline of the pseudo-bolometric light curve is slower than the deflagration model light curves. The spectroscopic features of SN 2020rea are typical of Type Iax SNe. The Si II line velocities of SN 2020rea are generally higher than those of other Type Iax SNe except for SNe 2011ay and 2012Z. The higher Fe line velocity than Si line around maximum indicates mixing of fully burned material. Spectral modelling of SN 2020rea shows weak Si II feature in early photospheric phase, an IGEs dominated ejecta ∼10 d after maximum and hints towards a mixed ejecta. The host galaxy metallicity (8.56 ± 0.18 dex) of SN 2020rea is similar to the host galaxy metallicity of SN 2012Z (8.51 ± 0.31 dex). Out of the several proposed explosion scenarios for Type Iax SNe, pure deflagration of white dwarf emerges as a promising one to explain the observed properties of SN 2020rea.

ACKNOWLEDGEMENTS

We thank the anonymous referee for giving constructive comments that has improved the presentation of the paper. We acknowledge Wiezmann Interactive Supernova data REPository http://wiserep.weizmann.ac.il (WISeREP; Yaron & Gal-Yam 2012). This research has made use of the CfA Supernova Archive, which is funded in part by the National Science Foundation through grant AST 0907903. This research has made use of the NASA/IPAC Extragalactic Database (NED) which is operated by the Jet Propulsion Laboratory, California Institute of Technology, under contract with the National Aeronautics and Space Administration. This work makes use of data obtained with the LCO Network. RD acknowledges funds by ANID grant FONDECYT Postdoctorado No. 3220449. KM acknowledges BRICS grant DST/IMRCD/BRICS/Pilotcall/ProFCheap/2017(G) for this work. The LCO group were supported by NSF grants AST-1911151 and AST-1911225. This research made use of TARDIS, a community-developed software package for spectral synthesis in supernovae (Kerzendorf et al. 2018, 2019). The development of TARDIS received support from the Google Summer of Code initiative and from ESA's Summer of Code in Space program. TARDIS makes extensive use of ASTROPY and PYNE. This work made use of the Heidelberg Supernova Model Archive (HESMA).[3]

DATA AVAILABILITY

The photometric and spectroscopic data of SN 2020rea presented in this paper will be made available by the corresponding author on request.

REFERENCES

Arnett W. D., 1982, ApJ, 253, 785
Barna B., Szalai T., Kromer M., Kerzendorf W. E., Vinkó J., Silverman J. M., Marion G. H., Wheeler J. C., 2017, MNRAS, 471, 4865
Barna B. et al., 2021, MNRAS, 501, 1078
Baron E., Höflich P., Krisciunas K., Dominguez I., Khokhlov A. M., Phillips M. M., Suntzeff N., Wang L., 2012, ApJ, 753, 105
Bobrick A., Zenati Y., Perets H. B., Davies M. B., Church R., 2022, MNRAS, 510, 3758
Bravo E., García-Senz D., 2006, ApJ, 642, L157
Bravo E., Gil-Pons P., Gutiérrez J. L., Doherty C. L., 2016, A&A, 589, A38
Brown T. M. et al., 2013, PASP, 125, 1031
Chatzopoulos E., Wheeler J. C., Vinko J., 2012, ApJ, 746, 121
Denissenkov P. A., Truran J. W., Herwig F., Jones S., Paxton B., Nomoto K., Suzuki T., Toki H., 2015, MNRAS, 447, 2696
Dessart L., Blondin S., Hillier D. J., Khokhlov A., 2014, MNRAS, 441, 532
Dutta A. et al., 2022, ApJ, 925, 217
Falco E. E. et al., 1999, PASP, 111, 438
Fernández R., Metzger B. D., 2013, ApJ, 763, 108
Fink M. et al., 2014, MNRAS, 438, 1762
Foley R. J. et al., 2009, AJ, 138, 376
Foley R. J. et al., 2013, ApJ, 767, 57
Foley R. J., McCully C., Jha S. W., Bildsten L., Fong W.-f., Narayan G., Rest A., Stritzinger M. D., 2014, ApJ, 792, 29
Foley R. J., Van Dyk S. D., Jha S. W., Clubb K. I., Filippenko A. V., Mauerhan J. C., Miller A. A., Smith N., 2015, ApJ, 798, L37
Foley R. J., Jha S. W., Pan Y.-C., Zheng W. K., Bildsten L., Filippenko A. V., Kasen D., 2016, MNRAS, 461, 433
Fox O. D. et al., 2016, ApJ, 816, L13
Gamezo V. N., Khokhlov A. M., Oran E. S., Chtchelkanova A. Y., Rosenberg R. O., 2003, Science, 299, 77

[3]https://hesma.h-its.org

Graur O., Bianco F. B., Modjaz M., Shivvers I., Filippenko A. V., Li W., Smith N., 2017, ApJ, 837, 121
Guevel D., Hosseinzadeh G., 2017, dguevel/PyZOGY: Initial Release. Available at: http://dx.doi.org/10.5281/zenodo.1043973
Hoeflich P., Khokhlov A., 1996, ApJ, 457, 500
Hoeflich P., Khokhlov A. M., Wheeler J. C., 1995, ApJ, 444, 831
Höflich P., Gerardy C. L., Fesen R. A., Sakai S., 2002, ApJ, 568, 791
Ivanova L. N., Imshennik V. S., Chechetkin V. M., 1974, Ap&SS, 31, 497
Jacobson-Galán W. V. et al., 2019, MNRAS, 487, 2538
Jha S. W., 2017, in Alsabti A., Murdin P., eds, Handbook of Supernovae, Type Iax Supernovae. Springer International Publishing AG, New York, p. 375
Jha S., Branch D., Chornock R., Foley R. J., Li W., Swift B. J., Casebeer D., Filippenko A. V., 2006, AJ, 132, 189
Jordan IV G. C., Perets H. B., Fisher R. T., van Rossum D. R., 2012, ApJ, 761, L23
Jordi K., Grebel E. K., Ammon K., 2006, A&A, 460, 339
Karambelkar V. R. et al., 2021, ApJ, 921, L6
Kashyap R., Haque T., Lorén-Aguilar P., García-Berro E., Fisher R., 2018, ApJ, 869, 140
Kawabata M. et al., 2018, PASJ, 70, 111
Kawabata M. et al., 2021, Publ. Astron. Soc. Japan, 73, 1295
Kerzendorf W. E., Sim S. A., 2014, MNRAS, 440, 387
Kerzendorf W. et al., 2018, tardis-sn/tardis: TARDIS v2.0.2 release
Kerzendorf W. et al., 2019, tardis-sn/tardis: TARDIS v3.0 alpha2
Kewley L. J., Dopita M. A., 2002, ApJS, 142, 35
Khokhlov A. M., 1991a, A&A, 245, L25
Khokhlov A. M., 1991b, A&A, 245, 114
Khokhlov A. M., 1991c, A&A, 246, 383
Khokhlov A., Mueller E., Hoeflich P., 1993, A&A, 270, 223
Kromer M. et al., 2013, MNRAS, 429, 2287
Kromer M. et al., 2015, MNRAS, 450, 3045
Lach F., Callan F. P., Bubeck D., Röpke F. K., Sim S. A., Schrauth M., Ohlmann S. T., Kromer M., 2022, A&A, 658, A179
Li W. et al., 2003, PASP, 115, 453
Li W. et al., 2011, MNRAS, 412, 1441
Magee M. R. et al., 2017, A&A, 601, A62
Magee M. R., Sim S. A., Kotak R., Maguire K., Boyle A., 2019, A&A, 622, A102
Makarov D., Prugniel P., Terekhova N., Courtois H., Vauglin I., 2014, A&A, 570, A13
McCully C. et al., 2014a, Nature, 512, 54
McCully C. et al., 2014b, ApJ, 786, 134
McCully C. et al., 2022, ApJ, 925, 138
McGaugh S. S., 1991, ApJ, 380, 140
Moriya T., Tominaga N., Tanaka M., Nomoto K., Sauer D. N., Mazzali P. A., Maeda K., Suzuki T., 2010, ApJ, 719, 1445
Narayan G. et al., 2011, ApJ, 731, L11
Perez-Fournon I. et al., 2020, Trans. Name Server Discovery Rep., 2020-2463, 1
Pettini M., Pagel B. E. J., 2004, MNRAS, 348, L59
Phillips M. M. et al., 2007, PASP, 119, 360
Pilyugin L. S., Thuan T. X., 2005, ApJ, 631, 231
Poidevin F. et al., 2020, Trans. Name Ser. Class. Rep., 2020-2512, 1
Poznanski D., Prochaska J. X., Bloom J. S., 2012, MNRAS, 426, 1465
Pumo M. L. et al., 2009, ApJ, 705, L138
Raddi R. et al., 2019, MNRAS, 489, 1489
Rodrigo C., Solano E., 2020, in XIV.0 Scientific Meeting (virtual) of the Spanish Astronomical Society. p. 182
Sahu D. K. et al., 2008, ApJ, 680, 580
Schlafly E. F., Finkbeiner D. P., 2011, ApJ, 737, 103
Seitenzahl I. R. et al., 2013, MNRAS, 429, 1156
Shen K. J., Schwab J., 2017, ApJ, 834, 180
Shen K. J. et al., 2018, ApJ, 865, 15
Sim S. A. et al., 2013, MNRAS, 436, 333
Singh M. et al., 2018, MNRAS, 474, 2551
Srivastav S. et al., 2020, ApJ, 892, L24
Srivastav S. et al., 2022, MNRAS, 511, 2708
Stritzinger M. D. et al., 2014, A&A, 561, A146
Stritzinger M. D. et al., 2015, A&A, 573, A2
Szalai T. et al., 2015, MNRAS, 453, 2103
Tomasella L. et al., 2016, MNRAS, 459, 1018
Tomasella L. et al., 2020, MNRAS, 496, 1132
Valenti S. et al., 2008, MNRAS, 383, 1485
Valenti S. et al., 2009, Nature, 459, 674
Valenti S. et al., 2016, MNRAS, 459, 3939
Vennes S., Nemeth P., Kawka A., Thorstensen J. R., Khalack V., Ferrario L., Alper E. H., 2017, Science, 357, 680
Wang X. et al., 2009, ApJ, 699, L139
White C. J. et al., 2015, ApJ, 799, 52
Yamanaka M. et al., 2015, ApJ, 806, 191
Yaron O., Gal-Yam A., 2012, PASP, 124, 668

This paper has been typeset from a TEX/LATEX file prepared by the author.